Transmission amplitude through a Coulomb blockaded Majorana wire

Matthias Thamm ●[*] and Bernd Rosenow

Institut für Theoretische Physik, Universität Leipzig, Brüderstrasse 16, 04103 Leipzig, Germany

We study coherent electronic transport through a Coulomb blockaded superconducting Rashba wire in the cotunneling regime between conductance resonances. By varying an external Zeeman field the wire can be tuned into a topological regime, where nonlocal transport through Majorana zero modes is the dominant mechanism. We model coherent transport in the cotunneling regime by using a scattering matrix formalism, and find that the transmission amplitude has a maximum as a function of Zeeman field, whose height is proportional to the wire length. We relate the transmission amplitude to the Majorana correlation length, and argue that the Zeeman field and length dependence of the transmission amplitude are unique signatures for the presence of Majorana zero modes.

I. INTRODUCTION

In recent years, Majorana zero modes (MZMs) have attracted much attention as possible candidates for the realization of topologically protected quantum bits [1–3]. MZMs can arise as localized zero-energy excitations in topological superconductors under suitable conditions [4–7], and many of their predicted experimental signatures have been observed, for instance a zero-bias conductance peak [8–12] and the suppression of the even-odd splitting of Coulomb blockade resonances in the topological phase [13].

The topological nature of MZMs manifests itself in their nonlocal character [14,15]. We study how the nonlocality of the electronic state encoded by MZMs can be probed by phase coherent transport through a Coulomb blockaded wire with MZMs at its ends [16–22]. By embedding the Majorana wire into the arm of an electron interferometer, the amplitude of coherent transmission through the MZMs can be studied [23]. In a conductance valley in between Coulomb blockade peaks, the amplitude of the transmission through a Majorana wire is determined by the magnitude of the wave functions at the ends of the wire. For MZMs, the wave function has a large magnitude $\propto 1/\sqrt{\xi}$ near the wire end, where ξ denotes the Majorana correlation length. In contrast, if the transmission is dominated by transport through extended states, the magnitude of wave functions $\propto 1/\sqrt{L}$ depends on the wire length. Taking into account the decrease of the charging energy with wire length, in a conductance valley one expects an increase of coherent transmission $\propto L$ when entering the topological regime, a robust signature of MZMs which also allows us

to distinguish them from pseudo-MZMs [21,24–30], which can arise in the presence of a soft confinement at the wire ends. Details of the magnetic field dependence follow from the relation $1/\xi = \Delta_{p,\mathrm{ind}}/(\hbar v_F)$, where $\Delta_{p,\mathrm{ind}}$ is the topological p-wave superconducting gap, in agreement with results of a recent experiment [23].

II. MODEL

A. Setup

In this article we consider a one-dimensional Rashba wire in proximity to an s-wave superconductor and subject to a perpendicular magnetic field. This system can be tuned into a topological regime where it realizes MZMs at the ends of the wire [1,32–36]. We consider a setup depicted in Fig. 1 where a wire in the Coulomb blockade regime is tunnel coupled to leads at each end and embedded into one arm of an Aharonov-Bohm interferometer. Thus, the combination of wire and superconductor acts as a quantum dot. By adjusting
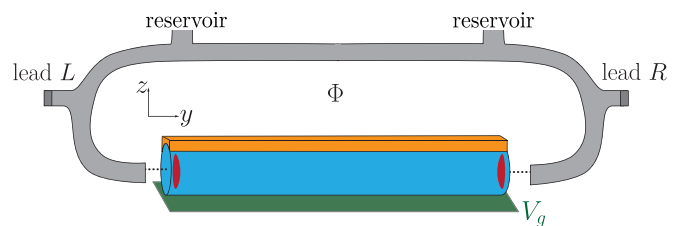

FIG. 1. Schematic sketch of the Majorana interferometer setup. The lower arm contains the quantum dot consisting of a one-dimensional Rashba wire (blue), superconductor (orange), and gate (green). The upper arm of the interferometer is the reference arm which only contains a wire. By varying a flux Φ, the transmission amplitude of electrons tunneling through the dot as a function of the gate voltage can be observed [22]. When the wire is tuned to the topological regime by an external Zeeman field, Majorana zero modes (red) are present at the ends. A reservoir is needed to avoid the phase rigidity effect [31].

*Corresponding author: thamm@itp.uni-leipzig.de

the flux Φ through the Aharonov-Bohm ring and measuring the conductance oscillations, it is possible to extract the complex transmission amplitude. Here we focus on the magnitude of the transmission amplitude, which includes phase information in the thermal average over occupations of the dot. For this reason, the transmission amplitude is able to distinguish MZMs from pseudo-MZMs, which is not possible when considering conductance measurements only.

B. Transmission amplitude

In lowest order interference, the current through the interferometer is given by

$$I(\Phi) \propto 2|T_{\mathrm{ref}}|^2 + \sum_{\sigma\sigma'} |T_{\sigma\sigma'}|^2 + 2 \sum_{\sigma} \mathrm{Re}[e^{i\Phi} T_{\mathrm{ref}} T_{\sigma\sigma}^*], \quad (1)$$

where T_{ref} is the transmission amplitude through the reference arm (assumed to be diagonal in spin). Here $T_{\sigma\sigma'}$ is the trans-

mission amplitude of coherently tunneling electrons with spin quantum number σ, σ', which is an entry of the scattering matrix determined by the Mahaux-Weidenmüller formula [37]

$$S = 1 - 2\pi i \left\langle W \frac{1}{\varepsilon - H_{\mathrm{eff}} + i\pi W^\dagger W} W^\dagger \right\rangle. \quad (2)$$

The brackets denote the thermal average over occupations $\{n_i\}$ of BdG eigenstates in the dot, defined as $\langle O \rangle = 1/Z \sum_{\{n_i\}} e^{-\beta E(\{n_i\})} O(\{n_i\})$. The average is performed for fixed total particle number N_0, which determines the number parity of occupied BdG levels $\{n_i\}$. Here ε is the energy of incoming electrons, and the effective dot Hamiltonian H_{eff} and the matrix of dot-lead couplings W with lead index α and spin σ are given by

$$H_{\mathrm{eff}} = \begin{pmatrix} \mathrm{diag}\big[\varepsilon_j^h(N_0, \{n_i\})\big]_{j=1,\ldots,j_{\max}} & 0 \\ 0 & \mathrm{diag}\big[\varepsilon_j^e(N_0, \{n_i\})\big]_{j=1,\ldots,j_{\max}} \end{pmatrix}, \quad (3)$$

$$(W)_{\alpha\sigma} = \sqrt{\varrho_F}\big[\lambda_{\alpha 1\sigma}^h(N_0, \{n_i\}), \ldots, \lambda_{\alpha j_{\max}\sigma}^h(N_0, \{n_i\}), \lambda_{\alpha 1\sigma}^e(N_0, \{n_i\}), \ldots, \lambda_{\alpha j_{\max}\sigma}^e(N_0, \{n_i\})\big]. \quad (4)$$

The energies for electron(hole)-like tunneling processes $\varepsilon_j^{e(h)}(N_0, \{n_i\})$ contain both charging energy and single particle energy levels of the wire Hamiltonian. To describe cotunneling processes, we consider the dot in an initial state $|N_0, \{n_i\}\rangle$. The transmission then occurs via an intermediate state $|N_0 \pm 1, \{n_i'\}\rangle$, where the allowed occupation numbers $\{n_i'\}$ of the intermediate state deviate from those of the initial state by adding or removing a single Bogolubon, and by adding (removing) one electron charge to the dot. The electron(hole)-like couplings $\lambda_{\alpha j\sigma}^{e(h)}(N_0, \{n_i\})$ of lead α to level j in the dot are obtained from the overlap $\langle N_0, \{n_i\}; \{\alpha, \sigma\}|H_{\mathrm{tun}}|N_0 \pm 1, \{n_i'\}\rangle$, with H_{tun} defined in Eq. (7).

In the topological regime, exponentially localized MZMs occur for instance at the left end of the wire with the wave function $\chi_{\sigma,L}(y)$ with envelop $\xi^{-1/2} e^{-y/\xi}$. In the presence of a small overlap between the left and right MZM, the BdG eigenfunctions are given by $(\chi_{\sigma,L} \pm \chi_{\sigma,R})/\sqrt{2}$. Evaluating Eq. (2) to leading order in the dot-lead couplings, one finds that the transmission amplitude through the MZMs is $T_{\sigma\sigma} \sim \chi_{\sigma,L}(y_L)\chi_{\sigma,R}^*(y_R)/(E_c/2)$. Thus, the transmission amplitude provides direct information about the Majorana localization length ξ.

C. Hamiltonian

We describe the proximitized semiconductor wire by the Hamiltonian

$$\mathcal{H}_{\mathrm{wire}} = \tau_z \otimes \left[-\frac{\hbar^2 \partial_y^2}{2m^*} \sigma_0 - \mu\sigma_0 - i\hbar\alpha_R \sigma_x \partial_y \right] - E_z \tau_0 \otimes \sigma_z + \Delta\tau_x \otimes \sigma_0. \quad (5)$$

Here τ_k and σ_k are Pauli matrices in particle-hole and spin space, respectively, and the Nambu basis spinor is given by

$[d_\uparrow^\dagger(y), d_\downarrow^\dagger(y), d_\downarrow(y), -d_\uparrow(y)]$. The parameter m^* is the effective mass of the electrons in the wire, α_R is the Rashba spin-orbit coupling strength, E_z is the Zeeman energy due to the perpendicular magnetic field B_z, and Δ is the proximity induced s-wave superconducting gap, which we choose to be real. The operator $d_j^\dagger$ creates an electron in the jth eigenstate of H_{wire} in the absence of superconductivity. We treat the charging term

$$H_{\mathrm{ch}} = \sum_j \left[-eV_g + \frac{E_c}{2} \sum_{i \neq j} d_i^\dagger d_i \right] d_j^\dagger d_j \quad (6)$$

in the Hartree approximation, which yields $E_c(N_0 - 1) - eV_g$ for the expectation value of the expression in brackets in case of a holelike cotunneling process, and $E_c N_0 - eV_g$ for an electronlike process. Here E_c is the charging energy needed to add an electron to the dot, which is proportional to the inverse of the wire length, and V_g is the gate voltage. Coupling between dot and leads is described by the tunneling Hamiltonian

$$H_{\mathrm{tun}} = \sum_{j\sigma\alpha} t_{\alpha j\sigma} c_\sigma^\dagger(y_\alpha) d_j + \mathrm{H.c.}, \quad (7)$$

where the couplings $t_{\alpha j\sigma} = t_0 \int dy \, \Psi_{\alpha,\sigma}(y) \varphi_j(y)$ are approximated as the overlap integral between a decaying wave $\Psi_{\alpha,\sigma}$ from lead α and the eigenfunction φ_j of the Hamiltonian H_{wire} for $\Delta = 0$ (see Appendix A). This approximation is relaxed later where we use a microscopic model to compute the couplings. In the topological regime, the weight of wave function $\Psi_{\alpha\uparrow}$ dominates over $\Psi_{\alpha\downarrow}$, such that the tunneling barrier effectively filters one spin direction [30]. In the first part we therefore focus on the transmission amplitude for spin-up electrons $|T_{\uparrow\uparrow}|$. From the Hamiltonians Eqs. (5)–(7) we determine the energies $\varepsilon_j^{e(h)}(N_0, \{n_i\})$ and couplings $\lambda_{\alpha j\sigma}^{e(h)}(N_0, \{n_i\})$ of lead α by numerically solving the BdG equation, combined

with analytical arguments for the spatial parity of wave functions (see Appendix A). We take into account the particle-hole redundancy in the solutions of the BdG equation by including only the eigenstates with positive energy [38]. The quantum dot contains an integer number N_0 of electrons. On the other hand, the particle number in the wire N_w is fractional in general. We therefore describe the proximity effect using a mean-field superconductivity term in the wire Hamiltonian, but distinguish N_0 from N_w [22].

The chemical potential μ is self-consistently determined such that the expectation value of the number of particles in the wire is given by N_w, but we take into account the total number of particles in the dot N_0 when we determine the charging contribution to the effective single particle energies. When varying the gate voltage one observes a conductance resonance whenever a level crosses the Fermi level. We increase N_0 by one after each such resonance. However, it is assumed that only a charge $\Delta N_w \ll 1$ is added to the wire.

D. Parameters

For the numerical calculations we use a spin orbit coupling strength of $\hbar\alpha_R = 0.2$ eV Å and an effective mass $m^* = 0.02\, m_e$, which are typical for semiconductor structures such as InAs [8,39]. From these parameters we obtain the characteristic energy and length scales $E_{\rm so} = \alpha_R^2 m^*/2 = 0.05$ meV and $l_{\rm so} = \hbar/(\alpha_R m^*) = 0.19\,\mu$m, respectively. We discretize the wire Hamiltonian Eq. (5) to N lattice sites with lattice constant $a = L/N = 0.026\, l_{\rm so}$, where L denotes the wire length. We assume that each electron that is added to the dot contributes a charge $\Delta N_w = 1/20$ to the wire. We use a charging energy $E_c = 8\, E_{\rm so}\,(32.5\, l_{\rm so})/L$. For computing the average of the scattering matrix Eq. (2) we use finite temperature $T = 34$ mK [23] corresponding to $\beta = 18\, E_{\rm so}$.

III. MAGNETIC FIELD DEPENDENCE OF THE TRANSMISSION AMPLITUDE

A. Magnetic field independent induced gap

We consider the transmission amplitude $|T_{\uparrow\uparrow}(V_{g,{\rm mid}})|$ as a function of Zeeman energy E_z, computed at a gate voltage $V_{g,{\rm mid}}$ in the middle between the two conductance resonances for a fixed particle number $N_w = (L/l_{\rm so})(14/13)$, such that the particle density is the same for all wire lengths.

We first consider a magnetic field independent proximity gap $\Delta = 2\, E_{\rm so}$. By increasing E_z, the transition to the topological phase takes place, in which an eigenstate close to zero energy is formed, separated from the second level by the topological gap (see Fig. 2). The transmission amplitude strongly increases when entering the topological phase at $E_{z,{\rm top}}$, reaches a peak value, and then decreases. In the topological regime the tunneling matrix element for a Majorana wave function is $\propto 1/\sqrt{\xi}$, where the correlation length

$$\xi = \frac{\hbar v_F}{\Delta_{p,{\rm ind}}}, \qquad (8)$$

with $v_F = \hbar k_F[1/m^* - \alpha_R^2(E_z^2 + \hbar^2\alpha_R^2 k_F^2)^{-1/2}]$, is determined by the induced effective p-wave gap at the Fermi points in the
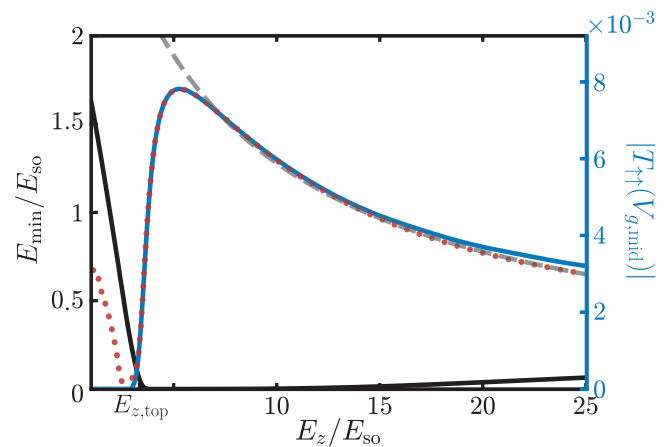

FIG. 2. Transmission amplitude $|T_{\uparrow\uparrow}(V_{g,{\rm mid}})|$ (blue y axis) for transmission through the lowest effective level only (dotted, red), and $j_{\max} = 200$ effective levels (solid, blue), together with the lowest BdG energy (black y axis, solid black line) of the wire Hamiltonian as a function of the magnetic field. Here $V_{g,{\rm mid}}$ is the center between amplitude resonances corresponding to a particle number $N_w = 35$. The dashed gray line shows the decay of the amplitude according to Eq. (10), where the constant factor is obtained from a fit. We use $\Delta = 2\, E_{\rm so}$ and $L = 32.5\, l_{\rm so}$.

hybrid wire [35,40,41]

$$\Delta_{p,{\rm ind}} = \frac{\hbar k_F \alpha_R \Delta}{\sqrt{E_z^2 + \alpha_R^2 \hbar^2 k_F^2}}. \qquad (9)$$

With this, we obtain the Zeeman field dependence of the transmission amplitude as

$$|T_{\uparrow\uparrow}| \sim \frac{m^*\alpha_R \Delta}{\hbar} \frac{1}{\sqrt{E_z^2 + \alpha_R^2 \hbar^2 k_F^2} - \alpha_R^2 m^*}, \qquad (10)$$

proportional to the inverse field strength for large E_z (dashed gray line in Fig. 2, in very good agreement with the numerical result taking a single level into account). When comparing the result for transmission through $j_{\max} = 200$ levels (solid blue line) with that for a single level (Fig. 2, dotted red line) it becomes apparent that the amplitude at the beginning of the topological range is mostly determined by the lowest level, i.e., the MZMs. For very large Zeeman energy, the Majorana modes are split more strongly, and there is a small correction due to taking into account many higher levels. In the trivial regime for $E_z < E_{z,{\rm top}}$ however, where the spacing between the lowest energy Bogolubons is small, many levels contribute to the transmission amplitude, and interfere destructively.

B. Magnetic field dependent induced gap

For a thin superconductor subject to a parallel field, we describe the suppression of the induced s-wave superconducting gap by the magnetic field via [42]

$$\Delta(E_z) = \Delta(0)\left[1 - \left(\frac{E_z}{E_{z,c}}\right)^2\right]^{1/2}, \qquad (11)$$

where $E_{z,c}$ is the critical Zeeman energy at which superconductivity is destroyed. Entering the topological region at $E_{z,{\rm top}}$
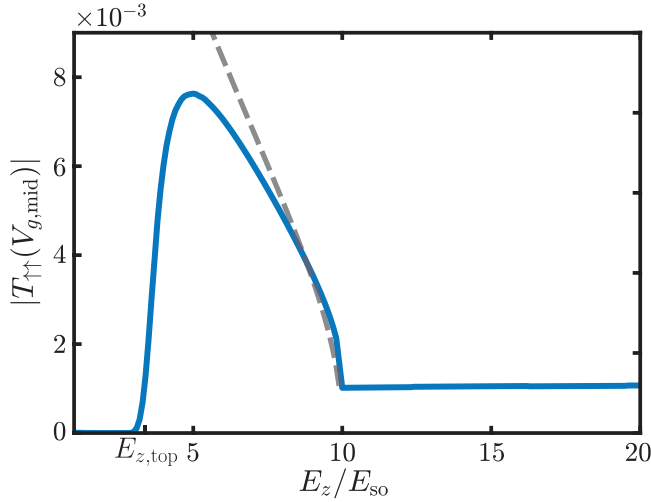
FIG. 3. Transmission amplitude $|T_{\uparrow\uparrow}(V_{g,\text{mid}})|$ for $j_{\text{max}} = 200$ effective levels as a function of the magnetic field. Here $V_{g,\text{mid}}$ is the center between amplitude resonances corresponding to a particle number $N_w = 35$. We use a wire length of $L = 32.5\,l_{\text{so}}$ and a field dependent induced gap Eq. (11) where $\Delta(4.5\,E_{\text{so}}) = 2\,E_{\text{so}}$ and $E_{z,c} = 10\,E_{\text{so}}$ (solid, blue). The dashed gray line shows the decay of the amplitude according to Eq. (12), where the constant factor is obtained from a fit.

is again accompanied by an increase in transmission amplitude (see Fig. 3). Further within the topological regime, the proximity gap Δ is reduced, and the correlation length $\xi \propto 1/|\Delta_{p,\text{ind}}|$ increases, i.e., the Majorana wave function delocalizes. Therefore, the amplitude drops to the normal-conducting value over a relatively narrow range of magnetic field values. Using Eq. (11) in Eq. (9), we find an amplitude dependence

$$|T_{\uparrow\uparrow}| \sim \frac{m^* \alpha_R \Delta(0)}{\hbar} \frac{\sqrt{1 - (E_z/E_{z,c})^2}}{\sqrt{E_z^2 + \alpha_R^2 \hbar^2 k_F^2} - \alpha_R^2 m^*}. \quad (12)$$

This dependence is depicted by the dashed gray line and fits well in the region where the amplitude decays to the normal-conducting value (see Fig. 3). For $E_z > E_{z,c}$, the wire is normal conducting, and the amplitude is approximately constant. These results for the amplitude are in agreement with the recent experiment [23].

C. Wire length dependence

The nonlocality of MZMs is expected to have a profound consequence when considering wires of varying lengths. In the inset of Fig. 4, the value of the amplitudes at the maximum and in the normal-conducting region are depicted as a function of the wire length L. From our scattering matrix analysis using a charging energy that is proportional to the inverse of the wire length, we find that the transmission amplitude is indeed proportional to the wire length in the topological region, while it is independent of the wire length in the normal-conducting range (see Fig. 4).
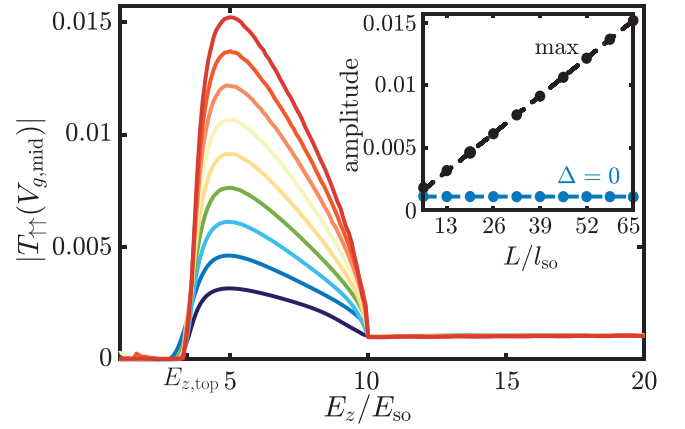

FIG. 4. Transmission amplitude $|T_{\uparrow\uparrow}(V_{g,\text{mid}})|$ as a function of the magnetic field for different wire lengths $L = 13\,l_{\text{so}}$, $19.5\,l_{\text{so}}$, $26\,l_{\text{so}}$, $32.5\,l_{\text{so}}$, $39\,l_{\text{so}}$, $45.5\,l_{\text{so}}$, $52\,l_{\text{so}}$, $58.5\,l_{\text{so}}$, and $65\,l_{\text{so}}$. Here $V_{g,\text{mid}}$ is the center between amplitude resonances for a particle number $N_w = 35L/(32.5\,l_{\text{so}})$. We assume a Zeeman field dependent gap parameter Eq. (11) with $\Delta(4.5\,E_{\text{so}}) = 2\,E_{\text{so}}$ and a critical field $E_{z,c} = 10E_{\text{so}}$. The inset shows the value at the maximum of the amplitude in the topological region (black circles) and the value of the amplitude in the normal-conducting region (blue circles) as a function of the wire length L.

IV. DISORDER IN THE WIRE

The proposed experiment for establishing the wire length dependence of the transmission amplitude in the presence or absence of MZMs requires the comparison of different wires. Since these wires may differ from each other in terms of their detailed composition, we study how robust our results for the transmission amplitude are in the presence of on-site disorder. We use a Gaussian disorder distribution with zero mean and standard deviation W. Disorder is strong when the elastic scattering rate $\hbar/\tau$ from the impurities is on the order of the induced effective gap $\Delta_{p,\text{ind}}$ in the wire [43–50]. We define a critical disorder strength W_m such that the effect of disorder on the amplitude is negligible for $W \ll W_m$. For $W \approx W_m$ disorder has noticeable effects on the amplitude and for $W \gg W_m$ pair breaking sets in and destroys the superconducting properties and the amplitude vanishes. Using Fermi's golden rule, we estimate the elastic scattering rate for the case of a scatterer at each lattice site as

$$\frac{\hbar/\tau}{E_{\text{so}}} = \left(\frac{W}{E_{\text{so}}}\right)^2 \frac{a}{l_{\text{so}}} \frac{1}{k_F l_{\text{so}}}. \quad (13)$$

The induced gap at the Fermi momentum $k_F l_{\text{so}} = \{2 + \mu/E_{\text{so}} + [(E_z/E_{\text{so}})^2 + 4 + 4\mu/E_{\text{so}}]^{1/2}\}^{1/2}$ is given by

$$\frac{\Delta_{p,\text{ind}}}{E_{\text{so}}} = 2\frac{\Delta}{E_{\text{so}}} \frac{k_F l_{\text{so}}}{\sqrt{(E_z/E_{\text{so}})^2 + 4(k_F l_{\text{so}})^2}}. \quad (14)$$

We define W_m such that $\hbar/\tau = \Delta_{p,\text{ind}}$ for $W = W_m$, i.e.,

$$\frac{W_m}{E_{\text{so}}} = \sqrt{2\frac{l_{\text{so}}}{a}\frac{\Delta}{E_{\text{so}}} \frac{k_F l_{\text{so}}}{[(E_z/E_{\text{so}})^2 + 4(k_F l_{\text{so}})^2]^{1/4}}}. \quad (15)$$

Numerical results of the amplitude for various disorder strengths are depicted in Fig. 5. When the disorder strength
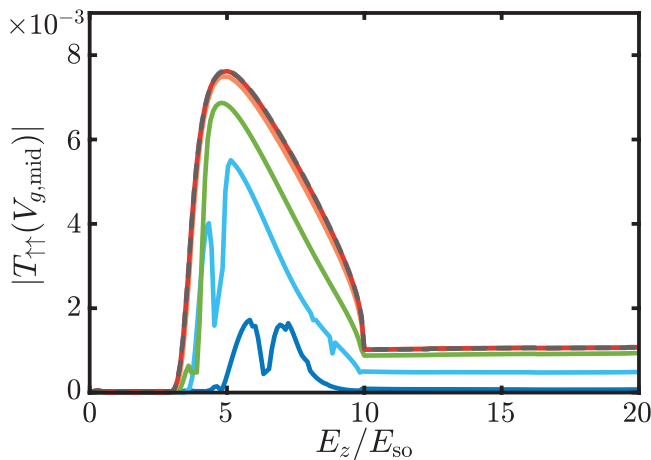
FIG. 5. Transmission amplitude $|T_{\uparrow\uparrow}(V_{g,\mathrm{mid}})|$ as a function of the magnetic field for various strength of on-site disorder. We use a wire length of $L = 32.5\,l_{\mathrm{so}}$ and compute the amplitude between resonances corresponding to particle number $N_w = 35$. The gray dashed line is for reference without disorder. The colored lines (from top to bottom) are numerically computed for Gaussian disorder with standard deviation $W = 0.1\,E_{\mathrm{so}} \ll W_{\mathrm{m}}$, $W = 1\,E_{\mathrm{so}}$, $W = 5\,E_{\mathrm{so}}$, $W = 10\,E_{\mathrm{so}} \sim W_{\mathrm{m}}$, and $W = 20\,E_{\mathrm{so}}$.

is smaller but of the order of W_{m}, the transmission amplitude is reduced at its maximum. This reduction is however much smaller that the peak height such that the proposed experiment is robust against disorder $W < W_{\mathrm{m}}$. When using a disorder strength close to or larger than W_{m}, the amplitude is significantly reduced.

V. MICROSCOPIC MODEL FOR COUPLINGS

In the first part we assumed that the couplings between lead and dot are determined by the dot wave functions at the ends of the wire. To validate this assumption we consider a tight-binding model of leads and wire which are separated by tunnel barriers of shape $V_{\sigma_i, V_0}(y) = V_0 \exp[-y^2/(2\sigma_i^2)]$. The potential at the left lead is given by

$$V(y) = \begin{cases} V_{\sigma_1, V_0 + V_{\mathrm{lead}}}(y - L_{\mathrm{lead}}) - V_{\mathrm{lead}}, & y \leqslant L_{\mathrm{lead}}, \\ V_{\sigma_1, V_0}(y - L_{\mathrm{lead}}), & L_{\mathrm{lead}} < y < y_1, \\ V_{\sigma_2, V_0}(y - y_1 + y_2 - L_{\mathrm{lead}}), & y \geqslant y_1, \end{cases}$$
$$y_j = \sqrt{2\sigma_j^2 \ln(V_0/E_s)}, \qquad (16)$$

where L and L_{lead} are the length of wire and leads, respectively. The potential in the leads is lowered by an offset $V_{\mathrm{lead}} = 100\,E_{\mathrm{so}}$, such that both spin directions are present at the Fermi level. The leads are normal conducting and without spin-orbit coupling. In the wire the potential consists of two parts with standard deviations σ_1 and σ_2 which are matched continuously at (y_1, E_s) by shifting the second peak by $y_1 - y_2$.

We define microscopic couplings as matrix elements $\lambda_{\alpha i \sigma}^u = \langle \Phi_{\alpha\sigma}^u | H | \Psi_i \rangle$ and $\lambda_{\alpha i \sigma}^v = \langle \Phi_{\alpha\sigma}^v | H | \Psi_i \rangle$ of the combined Hamiltonian of wire and leads. Here Ψ_i is the ith BdG level in the wire, and due to the particle-hole symmetry and the absence of superconductivity in the

leads we can write $\Phi_{\alpha\sigma}^u = (\varphi_{\alpha\uparrow}^{(\varepsilon_F, \sigma)}, \varphi_{\alpha\downarrow}^{(\varepsilon_F, \sigma)}, 0, 0)$ and $\Phi_{\alpha\sigma}^v = (0, 0, \varphi_{\alpha\downarrow}^{(\varepsilon_F, \sigma)*}, -\varphi_{\alpha\uparrow}^{(\varepsilon_F, \sigma)*})$ where $(\varphi_{\alpha\uparrow}^{(\varepsilon_F, \sigma)}, \varphi_{\alpha\downarrow}^{(\varepsilon_F, \sigma)})$ is the wave function localized in lead α with spin σ that is closest to the Fermi level. To numerically obtain the wave function localized in one region, we fix the potential at height V_0 in all the other regions. Figure 6 depicts the couplings between lead and first dot level for spin-$\uparrow$ and spin-$\downarrow$ electrons. For both types of confinement, the couplings of spin-$\uparrow$ electrons are dominant. It is therefore justified to only consider $|T_{\uparrow\uparrow}|$ in the more paradigmatic model in the first part. Due to the effective time-reversal symmetry $T = \sigma_z K$ with K denoting complex conjugation $T^2 = +1$ and $[H, T] = 0$, the transmission amplitudes $T_{\uparrow\uparrow}$ and $T_{\downarrow\downarrow}$ both have the same phase (modulo π), such that the magnitude of the interference term in Eq. (1) is given by $|T_{\uparrow\uparrow} + T_{\downarrow\downarrow}|$. We compute this magnitude for various wire lengths.

We distinguish two types of barrier potentials (i) only a narrow Gaussian peak and (ii) a narrow Gaussian peak together with a potential decaying smoothly into the wire [see Fig. 7(a)]. Parameters for (i) the steep potential are given by $\sigma_1 = \sigma_2 = 0.1\,l_{\mathrm{so}}$, $E_s = V_0$, and $V_0 = 65\,E_{\mathrm{so}}$, and for (ii) the smooth confinement $\sigma_1 = 0.1\,l_{\mathrm{so}}$, $\sigma_2 = 6\,l_{\mathrm{so}}$, $E_s = 10\,E_{\mathrm{so}}$, and $V_0 = 65\,E_{\mathrm{so}}$. In case (i) there are zero-energy states only in the topological region, which are the MZMs [see inset of Fig. 7(b)]. In case (ii), the Fourier decomposition of the smooth potential does not contain large momenta, so that in the trivial region each of the two bands contributes a pair of MZMs, which however are not coupled among each other by the potential [24,25,30]. Therefore, in addition to the MZMs in the topological region, two quasidegenerate, quasizero-energy Andreev bound states (also called pseudo-MZMs) occur in the trivial region for $5\,E_{\mathrm{so}} < E_z < 7.6\,E_{\mathrm{so}}$ [see inset of Fig. 7(b)]. Since they are nearly degenerate, there are two ground states with equal Boltzmann weight in the thermal average. For even N_0 the degenerate ground states for $\mathcal{E}_1 = \mathcal{E}_2 = 0$ are states where either all N_0 electrons are in the condensate or $N_0 - 2$ electrons form the condensate and both pseudo-MZMs are occupied. In the case of odd N_0 there are $N_0 - 1$ electrons in the condensate and either the first or the second pseudo-Majorana level is occupied. In both cases the thermally averaged amplitude is proportional to $\sum_{j=1}^{2}(\lambda_{L,j,\uparrow}^u \lambda_{R,j,\uparrow}^{u*} + \lambda_{L,j,\uparrow}^v \lambda_{R,j,\uparrow}^{v*}) \approx 0$. The antiunitary reflection symmetry $\tilde{\Pi}\varphi_j(y) = K\varphi_j(L - y)$ (where φ_j are eigenfunctions of H_{wire}) ensures that both terms are real and $\mathrm{sgn}(\lambda_{L,j,\uparrow}^u \lambda_{R,j,\uparrow}^{u*}) = -\mathrm{sgn}(\lambda_{L,j,\uparrow}^v \lambda_{R,j,\uparrow}^{v*})$ [22]. Due to the Majorana condition for zero-energy states $|u_{j\sigma}| = |v_{j\sigma}|$ the terms cancel each other. Hence, the ground state degeneracy gives rise to a vanishing amplitude upon thermal averaging [21]: Forming a Cooper pair or occupying the two zero-energy pseudo-MZMs requires the same energy, but yields contributions with opposite signs and equal magnitude to the transmission amplitude. For a wire of finite length, the pseudo-Majorana modes do not lie exactly at zero energy and a finite amplitude is observed. This is the case for the smallest wire length in Fig. 8(a). As long as the two levels are nearly degenerate and nearly at zero energy, the amplitude is well below the $\Delta = 0$ value and no pronounced maximum is formed. In addition, the amplitude is not proportional to L in the pseudo-MZM regime.
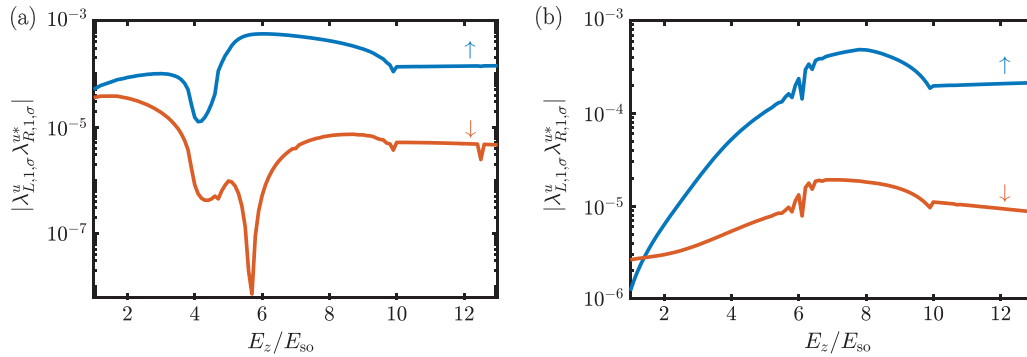
FIG. 6. Dot-lead couplings for both spin directions using a wire of length $L = 45.5 \, l_{so}$. We use the Zeeman field dependent induced gap $\Delta(E_z)$ Eq. (11) with a critical field $E_{z,c} = 10 \, E_{so}$. (a) Couplings to the lowest dot level using the steep potential and particle number $N_w = 47L/(39 \, l_{so})$ in the wire. (b) Couplings to the lowest dot level using the smooth potential for $N_w = 53L/(39 \, l_{so})$.

In comparison with the more paradigmatic model considered before, we find that for a steep potential (i) all qualitative features of the amplitude remain unchanged [Fig. 7(b)]. Importantly, the suppression of the transmission amplitude in the trivial regime occurs even when pseudo-MZMs are present [see Fig. 8(b)].

VI. COMPARISON BETWEEN INTERFEROMETER SETUP AND DIRECT CONDUCTANCE MEASUREMENT

In this section we compare signatures from the interferometer setup (Fig. 1), with an easier to implement direct conductance measurement through the dot, without interferometer. In the calculation of the transmission amplitude through the dot (interferometer case) or the transmission probability (direct conductance), the main difference is how the thermal average is performed. For the calculation of the amplitude of conductance oscillations through the interferometer, the thermal average is performed over the complex transmission amplitude [see Eq. (2)], so that the transmission phase contributes to such an average. In the case of a direct conductance measurement, the squared absolute value of the transmission amplitude is averaged, and the phase information does not contribute. Figure 8(b) depicts the direct conductance through the dot for a smooth confinement potential, analogous to Fig. 8(a). For MZMs we also find a maximum at the beginning of the topological region, whose height scales with the wire length. The crucial difference is that the conductance is not suppressed for pseudo-MZMs and thus this maximum is not a unique signature for the presence of MZMs.

VII. CONNECTION TO EXPERIMENT

In a recent experiment by Whiticar *et al.* [23], the transmission amplitude through a Coulomb blockaded Majorana wire was measured as a function of the Zeeman field. The experimental transmission amplitude shows a rapid growth upon entering the topological regime, followed by a pronounced maximum. Here we discuss in detail how these features are explained by the localization properties of MZMs, which determine the transmission amplitude in the topological regime.

In the case of sufficiently long wires, in which the Majorana wave functions of opposite wire ends have negligible overlap, an analytical solution for the MZM wave functions
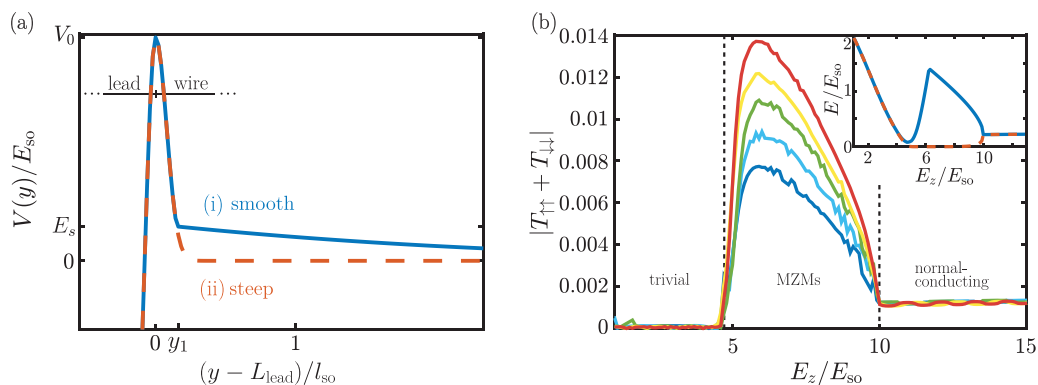

FIG. 7. (a) Barrier potential used to compute the lead-wire couplings in the microscopic model. The leads of length L_{lead} are normal conducting and without spin-orbit coupling. At position y_1 and energy E_s the narrow Gaussian peak transitions continuously into the wide peak in the case of the smooth potential. The height of the peak is given by $V_0 = 65 \, E_{so}$. (b) Numerical results for the amplitude $|T_{\uparrow\uparrow}(V_{g,mid}) + T_{\downarrow\downarrow}(V_{g,mid})|$ with microscopic couplings as a function of the Zeeman field using a steep confinement potential and ground state particle number $N_w = 47L/(39 \, l_{so})$. We consider wires of length $L = 32.5 \, l_{so}$, $39 \, l_{so}$, $45.5 \, l_{so}$, $52 \, l_{so}$, and $58.5 \, l_{so}$. The results are in good agreement with Fig. 4 where we used the more paradigmatic model for the couplings.
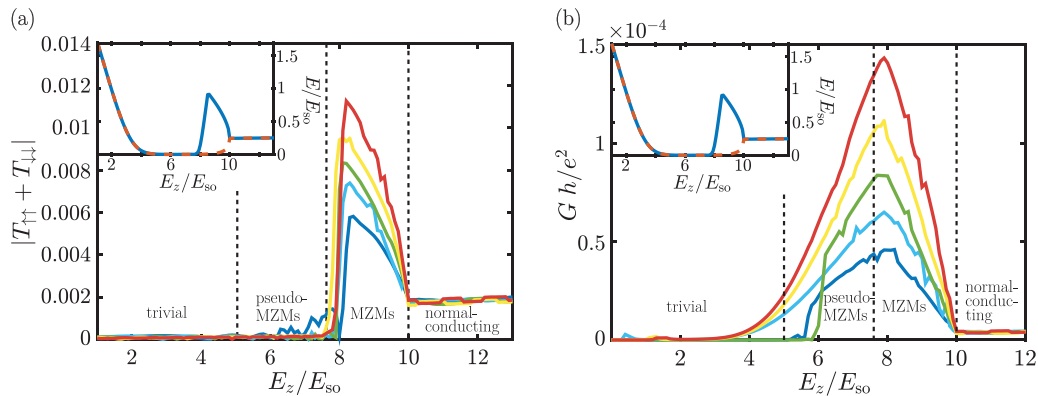
FIG. 8. (a) Numerical results for the transmission amplitude $|T_{\uparrow\uparrow}(V_{g,\mathrm{mid}}) + T_{\downarrow\downarrow}(V_{g,\mathrm{mid}})|$ using tunnel couplings obtained for the smooth barrier potential as a function of the Zeeman energy. (b) Conductance through the wire without an interferometer in the case of a smooth potential for $N_w = 53L/(39\,l_{\mathrm{so}})$. A comparison with (a) shows that the interferometer is crucial to distinguish MZMs from pseudo-MZMs. We consider wires of length $L = 32.5\,l_{\mathrm{so}}$, $39\,l_{\mathrm{so}}$, $45.5\,l_{\mathrm{so}}$, $52\,l_{\mathrm{so}}$, and $58.5\,l_{\mathrm{so}}$. We use a Zeeman field dependent induced gap Eq. (11) with a critical field $E_{z,c} = 10\,E_{\mathrm{so}}$ and a particle number $N_w = 53L/(39\,l_{\mathrm{so}})$. The insets depicts the lowest two energy eigenvalues of the wire Hamiltonian for $L = 45.5\,l_{\mathrm{so}}$.

can be found (see Appendix B). Moreover, since the transmission amplitude in the topological region is determined almost exclusively by transport through MZMs, the transmission amplitude can directly be obtained from the Majorana wave functions. In Sec. III we discussed that for large Zeeman fields, deep in the topological regime, the spatial decay of MZMs is characterized by the p-wave localization length $\xi = \hbar v_F/\Delta_{p,\mathrm{ind}}$ [Eq. (8)]. However, from the full analytic solution is is apparent that there is a second localization length

$$\xi_s = \left(-\xi^{-1} + \sqrt{\xi^{-2} - \frac{\mu^2 + \Delta^2 - E_z^2}{(\xi^{-2} + k_F^2)E_{\mathrm{so}}^2}}\right)^{-1}$$
$$\propto \frac{1}{E_z - \sqrt{\Delta^2 + \mu^2}}, \tag{17}$$

which describes the localization properties of MZMs for Zeeman fields $E_z \gtrsim E_{z,\mathrm{top}}$ close to the topological phase transition. We can approximate the envelope of the Majorana wave function by a sum of two exponentially decaying terms (for details see Appendix B)

$$\chi_{L,\uparrow} \approx \frac{1}{\sqrt{\xi + \xi_s}}(e^{-y/\xi} + e^{-y/\xi_s}). \tag{18}$$

The corresponding Majorana wave function at the right end is then given by $\chi_{R,\uparrow}(y) \propto \chi_{L,\uparrow}(L - y)$. This yields for the transmission amplitude

$$|T_{\uparrow\uparrow}(V_{g,\mathrm{mid}})| \propto \frac{1}{\xi + \xi_s}. \tag{19}$$

A comparison shows that the approximated transmission amplitude (dotted, red line in Fig. 9) is in very good agreement with the numerical results for transmission through 200 levels (solid, blue line in Fig. 9). Thus, the competition of the two correlation lengths ξ and ξ_s explains the occurrence of the maximum in the transmission amplitude.

In addition, in Fig. 9 we compare the numerically obtained transmission amplitude to approximations taking into account the larger of the two localization lengths: The behavior of the transmission amplitude at the beginning of the topological

region can be understood by the localization length ξ_s alone, i.e., $|T_{\uparrow\uparrow}| \propto 1/\xi_s$ (dashed gray line in the beginning of the topological regime). On the other hand, the behavior near the transition into the normal-conducting region is due to the p-wave localization length ξ, i.e., $|T_{\uparrow\uparrow}| \propto 1/\xi$ (dashed gray line at the end of the topological regime). The maximum occurs where the magnitude of the localization lengths is roughly comparable.

The picture described above allows us to explain the magnetic field dependence of transmission amplitude found by
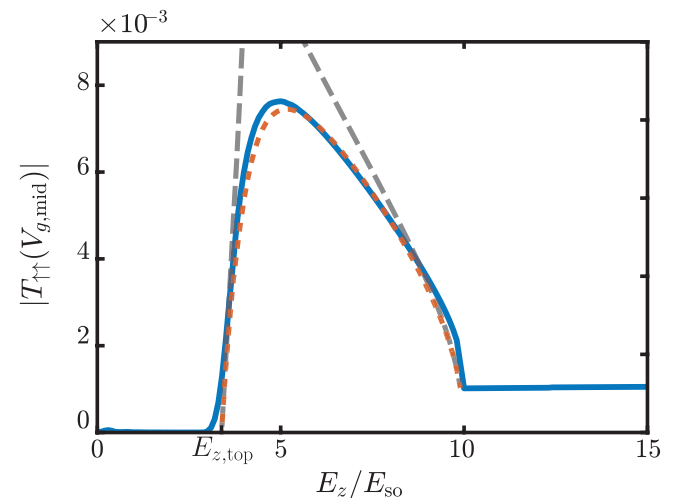

FIG. 9. Transmission amplitude $|T_{\uparrow\uparrow}(V_{g,\mathrm{mid}})|$ for $j_{\mathrm{max}} = 200$ effective levels (solid, blue) as a function of the magnetic field with parameters as in Fig. 3. The dashed gray lines depict the ξ_s approximation at the beginning of the topological regime and the ξ approximation in the region where superconductivity is destroyed by the magnetic field. The dotted red line depicts the approximation Eq. (19), where both correlation lengths are taken into account. The maximum of the transmission amplitude arises due to the interplay of both terms. We use the same proportionality constant for all three approximations obtained by a fit.

Whiticar *et al.* [23]. In the experiment, the transmission amplitude depends only weakly on the magnetic field in the region of small Zeeman fields, as predicted for the trivial phase. Above a device-specific value of the magnetic field, a rapid increase of the transmission amplitude is observed, which can be explained by the magnetic field dependence of $1/\xi_s$ at the beginning of the topological phase. Due to the divergence of ξ_s at the phase transition $E_z = E_{z,\text{top}}$, the transmission amplitude increases linearly $|T_{\uparrow\uparrow}| \propto E_z - E_{z,\text{top}}$ in the topological regime. For larger Zeeman fields, a well-defined maximum of the amplitude arises in the experiment, which can be understood in terms of the concurrence of both correlation lengths ξ and ξ_s. When superconductivity is destroyed by the magnetic field, Whiticar *et al.* observe a rapid decline of the transmission amplitude. This decrease can be explained in our model by the divergence of the coherence length ξ due to the vanishing of the induced *p*-wave gap when approaching the critical magnetic field.

Since the amplitude of coherent transmission does not exhibit a maximum in the case of pseudo-MZMs, we believe that it is very likely that genuine topological MZMs were observed in the experiment. This is further supported by the observation that together with the appearance of the maximum also the even-odd splitting of the conductance resonances is suppressed. While the behavior of the transmission amplitude in the topological regime can be understood with our one-dimensional model, it is currently not possible to explain the large ratio between the value of the transmission amplitude at the maximum and the value in the normal-conducting regime for device 2 measured by Whiticar *et al.* This could be because the amplitude in the experiment is not corrected for the influence of the transmission through the reference arm. On the other hand, it might be necessary to include the influence of orbital effects and several transverse subbands in the theoretical calculations for quantitative agreement between theory and experiment.

We believe that the experimental results are a promising step towards a proof for the presence of MZMs. Further evidence that MZMs can be consistently observed in these devices would be provided by a systematic study of wires with different lengths in future experiments.

VIII. CONCLUSION

We have studied coherent transport of electrons through a system hosting MZMs. We find that the Zeeman field and length dependence of the transmission amplitude provide unique signatures of MZMs. When considering wires of varying lengths, the nonlocality of MZMs yields a stable maximum of the amplitude at the onset of the topological regime, whose height is proportional to the wire length. In contrast, the amplitude is independent of the wire length if no localized MZM is present.

ACKNOWLEDGMENTS

APPENDIX A: DETAILS ON SCATTERING MATRIX FORMALISM

1. Truncation of the Hilbert space

As described in the main text, we do not explicitly model the superconductor but account for the proximity effect by including the induced superconducting gap directly into the Hamiltonian of the wire. However, we distinguish the particle number in the wire N_w from that in the dot N_0 consisting of wire and superconductor. Due to the Coulomb repulsion, simultaneous tunneling of more than one electron or hole is suppressed. We therefore truncate the Hilbert space to states of N_0 particles and states of $N_0 + 1$ electrons for electronlike cotunneling processes and $N_0 - 1$ for holelike cotunneling, respectively, but take into account many BdG eigenstates. We denote the occupation number of the jth BdG eigenstate by n_j. We introduce states $|N_0, \{n_i\}\rangle$ and $|N_0 \pm 1, \{n_i'\}\rangle$ where the former is the initial dot state with N_0 electrons and occupation of BdG quasiparticle states $\{n_i\}$. The latter is the intermediate, excited state with $N_0 \pm 1$ electrons, and occupation numbers $\{n_i'\}$. As a result of the mean-field treatment of the interaction in the BCS approach, the theory does not describe a definite particle number N_0 in the dot. However, fixed-N_0 superconducting systems can even in case of small N_0 be adequately described in the grand-canonical BCS theory by choosing the chemical potential μ such that the mean particle number $\langle \hat{N}_0 \rangle_\mu$ is given by N_0 [51]. We determine the chemical potentials self-consistently for the particle number N_w in the wire and use the dot particle number N_0 for computing the charging energy. We note that as the couplings only depend on N_w and since we evaluate the transmission amplitude for a gate voltage in between conductance resonances, which are determined by the lowest effective holelike and electronlike level, the amplitude does not depend on N_0 but only on N_w. We therefore define the self-consistently determined chemical potential $\mu \equiv \mu(N_0, \{n_i\})$ such that

$$
\langle \hat{N} \rangle_\mu \equiv \int dy \left[\sum_{j=1}^{2N} |\boldsymbol{v}_j(y, \mu)|^2 \right.
$$
$$
\left. + \sum_{j, \, n_j = 1} \left(-|\boldsymbol{v}_j(y, \mu)|^2 + |\boldsymbol{u}_j(y, \mu)|^2 \right) \right] = N_w.
\tag{A1}
$$

Here, due to the particle hole symmetry $P = \tau_y \otimes \sigma_y K$, we only need eigenfunctions with non-negative eigenenergies $\mathcal{E}_j(\mu) \geqslant 0$, which solve the BdG equation

$$
H_{\text{wire}}(\mu) \begin{pmatrix} \boldsymbol{u}_j(\mu) \\ \boldsymbol{v}_j(\mu) \end{pmatrix} = \mathcal{E}_j(\mu) \begin{pmatrix} \boldsymbol{u}_j(\mu) \\ \boldsymbol{v}_j(\mu) \end{pmatrix}.
\tag{A2}
$$

We rank order the energies and corresponding wave functions such that $\mathcal{E}_1 = \min\{\mathcal{E}_j\}$ and $\mathcal{E}_{j+1} > \mathcal{E}_j$. An important exception to this rule occurs when the wire is in the topological regime $|\mu| < \sqrt{E_z^2 - \Delta^2}$, where two Majorana subgap states are present in the full BdG spectrum. As the two Majorana wave functions overlap in a wire of finite length L, they hybridize to form a finite energy subgap BdG state $\mathcal{E}_1$. Increasing the chemical potential, one observes that this energy adiabatically evolves into a negative excitation energy $-|\mathcal{E}_1|$, which corresponds to a change in parity of the ground state.

We then need to take the solution with $\mathcal{E}_{-1} = -\mathcal{E}_1$ and $(\boldsymbol{u}_{-1}, \boldsymbol{v}_{-1}) = (\boldsymbol{v}_1^*, \boldsymbol{u}_1^*)$ as the lowest level, because it corresponds to the odd parity ground state in the topological regime [22]. We denote this solution again by $\mathcal{E}_1, (\boldsymbol{u}_1, \boldsymbol{v}_1)$ and use it for the corresponding chemical potentials in the computation of effective couplings and the effective energies.

We next express the wire and tunneling Hamiltonian in terms of BdG operators β_j. In order to do so, we first relate annihilation and creation operators $d_{j,\sigma}$, $d_{j,\sigma}^\dagger$ to eigenfunctions $\varphi_{j,\sigma}$ with spin σ of H_{wire} for $\Delta = 0$ via $d_{j,\sigma} = \sum_\sigma \int dy\, \varphi_{j,\sigma}^*(y)\Psi_\sigma(y)$. Using the expansion of field operators $\Psi_\sigma(y) = \sum_j e^{-i\frac{\phi}{2}}[u_{j\sigma}(y,\mu)\beta_j(\mu) + v_{j\sigma}^*(y,\mu)\beta_j^\dagger(\mu)]$ one finds

$$H_{\text{wire}} = \sum_{\substack{j \\ \mathcal{E}_j \geqslant 0}} \mathcal{E}_j(\mu)\beta_j^\dagger(\mu)\beta_j(\mu), \qquad (A3)$$

$$H_{\text{tun}} = \sum_{j\sigma\alpha} c_\sigma^\dagger(y_\alpha)e^{-i\frac{\phi}{2}}\big[\lambda_{j\alpha\sigma'}^u(\mu)\beta_j(\mu) \\ + \lambda_{j\alpha\sigma'}^v(\mu)\beta_j^\dagger(\mu)\big] + \text{H.c.} \qquad (A4)$$

Here the effective couplings are defined by

$$\lambda_{j\sigma\alpha}^u(\mu) = \sum_{i\sigma'} \int dy\, t_{i\alpha\sigma}\varphi_{i\sigma'}^*(y)u_{j\sigma'}(y,\mu),$$

$$\lambda_{j\sigma\alpha}^v(\mu) = \sum_{i\sigma'} \int dy\, t_{i\alpha\sigma}\varphi_{i\sigma'}^*(y)v_{j\sigma'}^*(y,\mu). \qquad (A5)$$

In the first part, the couplings $t_{\alpha j\sigma} = t_0 \int dy\, \Psi_{\alpha,\sigma}(y)\varphi_j(y)$ are approximated as the overlap integral between a decaying wave $\Psi_{\alpha,\sigma}$ from lead α and the eigenfunction φ_j of the Hamiltonian H_{wire} for $\Delta = 0$. We take $\Psi_{L,\sigma} \propto \exp(-y/\lambda)$ with $\lambda = 0.26\,l_{\text{so}}$ and similar for the right end. Since the couplings $t_{j\alpha\sigma}$ are therefore mostly determined by the values of the wave functions $\varphi_{j\sigma}(y)$ at the end y_α of the wire, and these wave function form an orthonormal set, the effective couplings are determined by the BdG wave functions $u_{j\sigma}$, $v_{j\sigma}$ at the ends of the wire. This is why we can relate the localization of the Majorana wave functions to the couplings that determine the transmission amplitude.

2. Coupling matrix elements and energy levels

To obtain the effective couplings $\lambda_{j\sigma\alpha}^e(\mu)$ $[\lambda_{j\sigma\alpha}^h(\mu)]$ for electron and holelike cotunneling processes, we consider a tunneling event in which the dot is initially in the state $|N_0, \{n_i\}\rangle$ and where cotunneling takes place via an excited state $|N_0 \pm 1, \{n_i'\}\rangle$. The couplings are given by the overlap $\langle N_0, \{n_i\}; \{\alpha, \sigma\}|H_{\text{tun}}|N_0 \pm 1, \{n_i'\}\rangle$. In principle we would need to consider overlap of condensate wave functions with different numbers of Cooper pairs, which however are not easily accessible in the BdG formalism. We hence neglect this contribution and use Eq. (A5) to determine the couplings, and we choose the chemical potential μ in the computation of the wave functions such that it corresponds to intermediate BdG state with $N_0 \pm 1$ electrons through which the tunneling occurs.

We separately consider electronlike and holelike processes and distinguish between even and odd particle number in

the ground state. As only pairs of electrons can enter the condensate of the superconductor, the transmission depends on the number parity of N_0. For even N_0, the $T = 0$ ground state is given by $|N_0, \{n_i = 0\}; \{\alpha, \sigma\}\rangle$, i.e., all electrons are in the condensate. For odd N_0 we assume that one electron resides in the first BdG eigenstate such that the ground state is given by $|N_0, \{n_1 = 1, n_{i\neq 1} = 0\}; \{\alpha, \sigma\}\rangle$. Electronlike intermediate states are $|N_0 + 1, \{n_m' = 1, n_{i\neq m}' = 0\}\rangle$ for even N_0 and $(|N_0 + 1, \{n_i' = 0\}\rangle, |N_0 + 1, \{n_1' = 1, n_m' = 1, n_{i\notin\{1,m\}}' = 0\}\rangle)$ for odd N_0. For holelike cotunneling, intermediate states have $N_0 - 1$ electrons and the occupancy of Bogolubons changes in an analogous way to the electron excited states described above. In this way we find the following effective couplings for $T = 0$:

$$\lambda_{\alpha,j,\sigma}^h(N_0, \{n_i\}) = \begin{cases} \lambda_{\alpha,j,\sigma}^u[\mu_j^h(\{n_i\})], & \text{for } n_j = 1, \\ \lambda_{\alpha,j,\sigma}^v[\mu_j^h(\{n_i\})], & \text{for } n_j = 0, \end{cases} \quad (A6)$$

$$\lambda_{\alpha,j,\sigma}^e(N_0, \{n_i\}) = \begin{cases} \lambda_{\alpha,j,\sigma}^v[\mu_j^e(\{n_i\})], & \text{for } n_j = 1, \\ \lambda_{\alpha,j,\sigma}^u[\mu_j^e(\{n_i\})], & \text{for } n_j = 0, \end{cases} \quad (A7)$$

where the superscript e denotes electronlike and h holelike couplings, α is a lead index, σ is the spin of the tunneling electron in the lead, and n_j is the state through which the tunneling occurs.

In addition, we consider excited initial states $|N_0, \{n_i\}\rangle$ with energy $E(\{n_i\}) = \sum_{j,n_j=1} \mathcal{E}_j$, whose statistical weight is described by the Boltzmann factor $e^{-\beta E(\{n_i\})}$ with $\beta = 1/k_B T$. For even N_0, an even number of BdG states has to be occupied, and an odd number of BdG states for odd N_0. Numerically computing the excitation energies reveals that excited states with occupied levels $n_{j>10} = 1$ have too small Boltzmann factors to significantly contribute to the transmission amplitude. We therefore restrict ourselves to excited states where only levels with energies among the ten smallest ones can be occupied. Also states with more than three occupied levels yield negligible weights and are therefore neglected. In addition, we do not recompute the chemical potential for each excited state and instead use the chemical potential of the respective $T = 0$ state.

In addition to the tunneling matrix elements, the effective energies of the intermediate states are needed. We find

$$\varepsilon_{\text{eff},j}^h = \begin{cases} +\mathcal{E}_j[\mu_j^h(\{n_i\})] - eV_g + E_c(N_0 - 1), & \text{for } n_j = 1, \\ -\mathcal{E}_j[\mu_j^h(\{n_i\})] - eV_g + E_c(N_0 - 1), & \text{for } n_j = 0, \end{cases}$$
$$(A8)$$

$$\varepsilon_{\text{eff},j}^e = \begin{cases} -\mathcal{E}_j[\mu_j^e(\{n_i\})] - eV_g + E_c N_0, & \text{for } n_j = 1, \\ +\mathcal{E}_j[\mu_j^e(\{n_i\})] - eV_g + E_c N_0, & \text{for } n_j = 0. \end{cases}$$
$$(A9)$$

Using these, we obtain the transmission amplitude from the scattering matrix Eq. (2) via $T_{\uparrow\uparrow} = S(1,3)$ and $T_{\downarrow\downarrow} = S(2,4)$. In the thermal average we define $Z = \sum_{\{n_i\}|N_0} e^{-\beta E(\{n_i\})}$ where the number parity of $\sum_i n_i$ is determined by the number parity of N_0. The antiunitary reflection symmetry $\tilde{\Pi}\varphi_j(y) = K\varphi_j(L-y)$ (where φ_j are eigenfunctions of H_{wire}) ensures that $T_{\sigma\sigma}$ is imaginary in the middle between resonances where the real part of the denominator $\approx E_c/2$ is large compared to the level broadening. We consider transmission through the first j_{max} levels.

APPENDIX B: ANALYTIC SOLUTION FOR MAJORANA WAVE FUNCTION

The BdG equations of a semi-infinite Rashba wire can in fact be solved analytically for an exact zero-energy state [52]. Therefore, assuming a sufficiently long wire such that the Majorana wave functions of both ends have negligible overlap, one can derive an analytical expression for the Majorana wave functions. In this Appendix we present the analytical solution and a series of approximations that help to understand the emergence of the maximum of the transmission amplitude at the onset of the topological regime.

The solution of the BdG equation $\mathcal{H}_{\mathrm{wire}}\psi = 0$, $\psi(0) = 0$ for a zero-energy state with $\mathcal{H}_{\mathrm{wire}}$ defined in Eq. (5) has the form $\psi = (\chi_\uparrow, \chi_\downarrow, i\chi_\downarrow, i\chi_\uparrow)$. By making use of the real functions $\exp(i\pi/4)\chi_\uparrow = \hat{\chi}_\uparrow \in \mathbb{R}$, $i\exp(i\pi/4)\chi_\downarrow = \hat{\chi}_\downarrow \in \mathbb{R}$ the BdG equation reduces to the two equations

$$-\partial_{\tilde{y}}^2\hat{\chi}_\uparrow - \tilde{\mu}\hat{\chi}_\uparrow - \tilde{E}_z\hat{\chi}_\uparrow - 2\partial_{\tilde{y}}\hat{\chi}_\downarrow + \tilde{\Delta}\hat{\chi}_\downarrow = 0,$$
$$-\partial_{\tilde{y}}^2\hat{\chi}_\downarrow - \tilde{\mu}\hat{\chi}_\downarrow + \tilde{E}_z\hat{\chi}_\downarrow + 2\partial_{\tilde{y}}\hat{\chi}_\uparrow - \tilde{\Delta}\hat{\chi}_\uparrow = 0,$$
(B1)

Here we use reduced quantities $\tilde{\mu} = \mu/E_{\mathrm{so}}$, $\tilde{E}_z = E_z/E_{\mathrm{so}}$, $\tilde{\Delta} = \Delta/E_{\mathrm{so}}$, $\tilde{y} = y/l_{\mathrm{so}}$, and $\tilde{k} = kl_{\mathrm{so}}$. Since Majorana modes are expected to be exponentially localized at the end of the semi-infinite wire, we use an ansatz

$$\begin{pmatrix} \hat{\chi}_\uparrow \\ \hat{\chi}_\downarrow \end{pmatrix} = e^{-A\tilde{y}}\begin{pmatrix} \varrho_\uparrow \\ \varrho_\downarrow \end{pmatrix}.$$
(B2)

With this ansatz we obtain the system of equations

$$\begin{pmatrix} -A^2 - \tilde{\mu} - \tilde{E}_z & 2A + \tilde{\Delta} \\ -2A - \tilde{\Delta} & -A^2 - \tilde{\mu} + \tilde{E}_z \end{pmatrix}\begin{pmatrix} \varrho_\uparrow \\ \varrho_\downarrow \end{pmatrix} = 0.$$
(B3)

The requirement for a nontrivial solution, i.e., a vanishing determinant of the coefficient matrix, yields the quartic equation

$$0 = A^4 + A^2(2\tilde{\mu} + 4) + A(4\tilde{\Delta}) + \tilde{\mu}^2 - \tilde{E}_z^2 + \tilde{\Delta}^2$$
(B4)

in A which is already in the reduced form $A^4 + A^2\alpha + A\beta + \gamma = 0$ and can be solved analytically. By factorizing the polynomial $0 = (A - A_1)(A - A_2)(A - A_3)(A - A_4)$ using its four roots, and comparing to the above equation, one finds that $0 = A_1 + A_2 + A_3 + A_4$ and $A_1A_2A_3A_4 = \tilde{\mu}^2 - \tilde{E}_z^2 + \tilde{\Delta}^2$. The four solutions are given by

$$A_i = \tfrac{1}{2}\left[\pm_1 W \pm_2 \sqrt{W^2 - 4(\alpha + Y \pm_1 Z)}\right],$$
(B5)

with the abbreviations $P = -\alpha^2/12 - \gamma$, $Q = -\alpha^3/108 + \alpha\gamma/3 - \beta^2/8$, $U = (-Q/2 + \sqrt{Q^2/4 + P^3/27})^{1/3}$, $Y = -5\alpha/6 + U - P/(3U)$, $W = \sqrt{\alpha + 2Y}$, and $Z = \beta/(2W)$. Here $\pm_1$ and $\pm_2$ can individually be $+1$ or -1 to give rise to four solutions A_i. In the topological regime $\gamma = \tilde{\mu}^2 - \tilde{E}_z^2 + \tilde{\Delta}^2 < 0$, it can be shown that a solution with $\mathrm{Re}A_1$, $\mathrm{Re}A_2$, $\mathrm{Re}A_3 > 0$, $A_1 = A_2^*$, $\mathrm{Im}A_3 = 0$, and $\mathrm{Re}A_4 < 0$ exists. To be able to normalize the solution, the coefficient of the A_4 term needs to vanish. Then, Eq. (B3) has the solution

$$\begin{pmatrix} \varrho_{\uparrow,i} \\ \varrho_{\downarrow,i} \end{pmatrix} = \mathcal{N}_i\begin{pmatrix} 2A_i + \tilde{\Delta} \\ A_i^2 + \tilde{\mu} + \tilde{E}_z \end{pmatrix},$$
(B6)

where $\mathcal{N}_i$ are normalization constants. In the topological regime we define

$$A_1 = \tilde{\xi}_1^{-1} + i\tilde{k}_{\mathrm{eff}},$$
(B7)

$$A_2 = \tilde{\xi}_1^{-1} - i\tilde{k}_{\mathrm{eff}},$$
(B8)

$$A_3 = \tilde{\xi}_2^{-1}.$$
(B9)

Therefore, the Majorana wave function

$$\hat{\boldsymbol{\chi}}_{\mathrm{L}}(y) = \mathcal{N}\Bigg[e^{-y/\xi_2}\begin{pmatrix} 2\tilde{\xi}_2^{-1} + \tilde{\Delta} \\ \tilde{\xi}_2^{-2} + \tilde{\mu} + \tilde{E}_z \end{pmatrix}$$
$$+ e^{-y/\xi_1}\Bigg\{ae^{i\tilde{k}_{\mathrm{eff}}y}\begin{pmatrix} 2(\tilde{\xi}_1^{-1} + i\tilde{k}_{\mathrm{eff}}) + \tilde{\Delta} \\ (\tilde{\xi}_1^{-1} + i\tilde{k}_{\mathrm{eff}})^2 + \tilde{\mu} + \tilde{E}_z \end{pmatrix}$$
$$+ be^{-i\tilde{k}_{\mathrm{eff}}y}\begin{pmatrix} 2(\tilde{\xi}_1^{-1} - i\tilde{k}_{\mathrm{eff}}) + \tilde{\Delta} \\ (\tilde{\xi}_1^{-1} - i\tilde{k}_{\mathrm{eff}})^2 + \tilde{\mu} + \tilde{E}_z \end{pmatrix}\Bigg\}\Bigg]$$
(B10)

consist of a evanescent term with localization length ξ_2 and an oscillating term with localization length of the envelop ξ_1. Here the boundary condition $\hat{\boldsymbol{\chi}}_{\mathrm{L}}(0) = 0$ fixes the coefficients

$$a = b^* = \frac{[i\tilde{\xi}_2 + \tilde{\xi}_1(-i + \tilde{k}_{\mathrm{eff}}\tilde{\xi}_2)][-2 + 2(\tilde{E}_z + \tilde{\mu})\tilde{\xi}_1\tilde{\xi}_2 - \tilde{\Delta}(\tilde{\xi}_1 + \tilde{\xi}_2) + i\tilde{k}_{\mathrm{eff}}\tilde{\xi}_1(2 + \tilde{\Delta}\tilde{\xi}_2)]}{4\tilde{k}_{\mathrm{eff}}\{1 + \tilde{\xi}_1[\tilde{\Delta} - (\tilde{E}_z - \tilde{k}_{\mathrm{eff}}^2 + \tilde{\mu})\tilde{\xi}_1]\}\tilde{\xi}_2^2}.$$
(B11)

In the following we refer to this solution as "analytic solution." To compute the transmission amplitude we use that the Majorana wave function at the right wire end is given by $\chi_R(y) \propto \chi_L^*(L - y)$ and evaluate the overlap with decaying wave functions from the leads.

We find that the analytic expression is in very good agreement with the numerical results (Fig. 10) in the topological regime, even when taking transport through many levels into account. However, without some approximations it is difficult to gain much insight into the lengthy analytical expression. In order to make progress, we first use that the oscillations of the Majorana wave functions is approximately determined by the Fermi momentum

$$k_{\mathrm{eff}} \approx \tilde{k}_F = \sqrt{2 + \tilde{\mu} + \sqrt{\tilde{E}_z^2 + 4 + 4\tilde{\mu}}},$$
(B12)

which is nearly independent of E_z in the case where the chemical potential is self-consistently determined to fix the particle number in the wire. In addition, the localization length of the oscillating term can be approximated by the coherence length due to the p-wave gap

$$\xi_1 = \mathrm{Re}(A_1)^{-1}l_{\mathrm{so}} \approx \xi = \frac{\hbar v_F}{\Delta_{p,\mathrm{ind}}}.$$
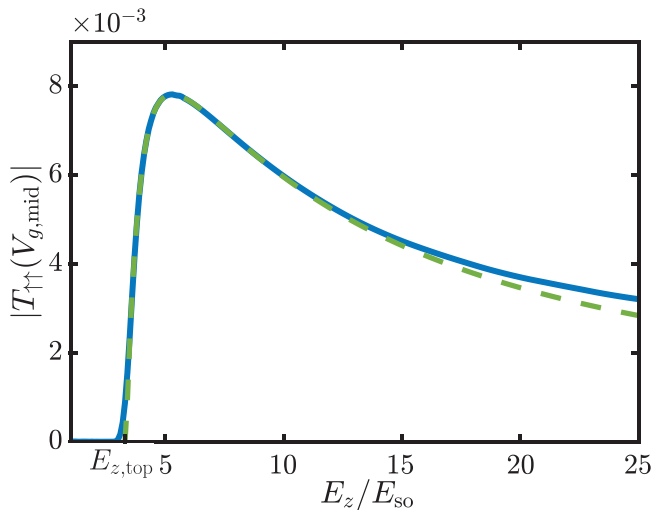(B13)

FIG. 10. Comparison between numerical result (solid, blue) for the transmission amplitude $|T_{\uparrow\uparrow}(V_{g,\text{mid}})|$ in the topological region as a function of the magnetic field for $j_{\text{max}} = 200$ level, $N_w = 35$ and $\Delta = 2\,E_{\text{so}}$ and full analytical solution (dashed, green), in very good agreement with the numerical result. For very large Zeeman energies, higher levels contribute to the transmission and the overlap between the MZMs from the ends is finite such that there is a small deviation between analytic and numeric results.

The evanescent term however, has a different correlation length whose divergence at the topological phase transition is governed by the closing of the topological gap at $E_z = E_{z,\text{top}}$,

$$\xi_2 = A_3^{-1} l_{\text{so}} \approx \xi_s = \left(-\xi^{-1} + \sqrt{\xi^{-2} - \frac{\tilde{\mu}^2 + \tilde{\Delta}^2 - \tilde{E}_z^2}{\xi^{-2} + k_F^2}} \right)^{-1}$$

$$\propto \frac{1}{E_z - \sqrt{\Delta^2 + \mu^2}}. \tag{B14}$$

Here we used the relations between the A_i above Eq. (B5) to express A_3 in terms of A_1, A_2 and ultimately in terms of ξ.
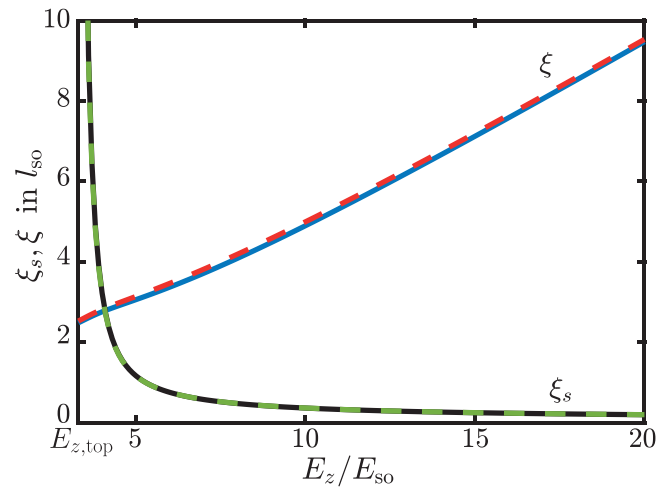

FIG. 11. Full analytic correlation lengths $\xi_1 = l_{\text{so}}\text{Re}(A_1)^{-1}$ and $\xi_2 = l_{\text{so}}\text{Re}(A_3)^{-1}$ (solid lines) and approximations ξ and ξ_s (dashed lines). Here we used the self-consistent chemical potential $\mu(E_z)$ for fixed particle number $N_w = 35$ in the wire and $\Delta = 2\,E_{\text{so}}$.

We find that the approximations for the localization lengths (dashed lines in Fig. 11) are in excellent agreement with the exact analytical expressions (solid lines in Fig. 11) in the whole topological regime. For the approximation in the main text, the Majorana wave functions are reduced to the sum of the envelops of oscillating and evanescent term, neglecting the spin dependence and the oscillations. As the couplings are determined by the wave function weights at the ends of the wire, the oscillations are less important. However, in the evanescent term, the spin-↓ component can be larger than the spin-↑ component at the beginning of the topological regime. Nevertheless, this rough approximation is still in good agreement with the numerical results for the case where k_F is approximately constant (as for a fixed particle number in the wire) and allows us to understand the occurrence of the amplitude maximum.

[1] J. Alicea, Y. Oreg, G. Refael, F. von Oppen, and M. P. A. Fisher, Non-Abelian statistics and topological quantum information processing in 1D wire networks, Nat. Phys. **7**, 412 (2011).

[2] T. Hyart, B. van Heck, I. C. Fulga, M. Burrello, A. R. Akhmerov, and C. W. J. Beenakker, Flux-controlled quantum computation with Majorana fermions, Phys. Rev. B **88**, 035121 (2013).

[3] D. J. Clarke, J. D. Sau, and S. Tewari, Majorana fermion exchange in quasi-one-dimensional networks, Phys. Rev. B **84**, 035120 (2011).

[4] J. Alicea, New directions in the pursuit of Majorana fermions in solid state systems, Rep. Prog. Phys. **75**, 076501 (2012).

[5] C. Beenakker, Search for Majorana fermions in superconductors, Annu. Rev. Condens. Matter Phys. **4**, 113 (2013).

[6] A. E. Antipov, A. Bargerbos, G. W. Winkler, B. Bauer, E. Rossi, and R. M. Lutchyn, Effects of Gate-Induced Electric Fields on Semiconductor Majorana Nanowires, Phys. Rev. X **8**, 031041 (2018).

[7] A. Schuray, D. Frombach, S. Park, and P. Recher, Transport signatures of Majorana bound states in superconducting hybrid structures, Eur. Phys. J.: Spec. Top. **229**, 593 (2020).

[8] V. Mourik, K. Zuo, S. M. Frolov, S. R. Plissard, E. P. A. M. Bakkers, and L. P. Kouwenhoven, Signatures of Majorana fermions in hybrid superconductor-semiconductor nanowire devices, Science **336**, 1003 (2012).

[9] M. T. Deng, C. L. Yu, G. Y. Huang, M. Larsson, P. Caroff, and H. Q. Xu, Anomalous zero-bias conductance peak in a Nb-InSb nanowire-Nb hybrid device, Nano Lett. **12**, 6414 (2012).

[10] A. Das, Y. Ronen, Y. Most, Y. Oreg, M. Heiblum, and H. Shtrikman, Zero-bias peaks and splitting in an Al-InAs nanowire topological superconductor as a signature of Majorana fermions, Nat. Phys. **8**, 887 (2012).

[11] A. D. K. Finck, D. J. Van Harlingen, P. K. Mohseni, K. Jung, and X. Li, Anomalous Modulation of a Zero-Bias Peak in a Hybrid Nanowire-Superconductor Device, Phys. Rev. Lett. **110**, 126406 (2013).

[12] H. O. H. Churchill, V. Fatemi, K. Grove-Rasmussen, M. T. Deng, P. Caroff, H. Q. Xu, and C. M. Marcus, Superconductor-nanowire devices from tunneling to the multichannel regime: Zero-bias oscillations and magnetoconductance crossover, Phys. Rev. B **87**, 241401(R) (2013).

[13] S. M. Albrecht, A. P. Higginbotham, M. Madsen, F. Kuemmeth, T. S. Jespersen, J. Nygård, P. Krogstrup, and C. M. Marcus, Exponential protection of zero modes in Majorana islands, Nature (London) **531**, 206 (2016).

[14] C. Nayak, S. H. Simon, A. Stern, M. Freedman, and S. Das Sarma, Non-Abelian anyons and topological quantum computation, Rev. Mod. Phys. **80**, 1083 (2008).

[15] A. Stern, Anyons and the quantum Hall effect—A pedagogical review, Ann. Phys. **323**, 204 (2008).

[16] L. Fu, Electron Teleportation via Majorana Bound States in a Mesoscopic Superconductor, Phys. Rev. Lett. **104**, 056402 (2010).

[17] L. A. Landau, S. Plugge, E. Sela, A. Altland, S. M. Albrecht, and R. Egger, Towards Realistic Implementations of a Majorana Surface Code, Phys. Rev. Lett. **116**, 050501 (2016).

[18] S. Plugge, L. A. Landau, E. Sela, A. Altland, K. Flensberg, and R. Egger, Roadmap to Majorana surface codes, Phys. Rev. B **94**, 174514 (2016).

[19] S. Vijay and L. Fu, Teleportation-based quantum information processing with Majorana zero modes, Phys. Rev. B **94**, 235446 (2016).

[20] S. Plugge, A. Rasmussen, R. Egger, and K. Flensberg, Majorana box qubits, New J. Phys. **19**, 012001 (2017).

[21] M. Hell, K. Flensberg, and M. Leijnse, Distinguishing Majorana bound states from localized Andreev bound states by interferometry, Phys. Rev. B **97**, 161401(R) (2018).

[22] C. Drukier, H.-G. Zirnstein, B. Rosenow, A. Stern, and Y. Oreg, Evolution of the transmission phase through a Coulomb-blockaded Majorana wire, Phys. Rev. B **98**, 161401(R) (2018).

[23] A. M. Whiticar, A. Fornieri, E. C. T. O'Farrell, A. C. C. Drachmann, T. Wang, C. Thomas, S. Gronin, R. Kallaher, G. C. Gardner, M. J. Manfra, C. M. Marcus, and F. Nichele, Coherent transport through a Majorana island in an Aharonov-Bohm interferometer, Nat. Commun. **11**, 3212 (2020).

[24] E. Prada, P. San-Jose, and R. Aguado, Transport spectroscopy of NS nanowire junctions with Majorana fermions, Phys. Rev. B **86**, 180503(R) (2012).

[25] G. Kells, D. Meidan, and P. W. Brouwer, Near-zero-energy end states in topologically trivial spin-orbit coupled superconducting nanowires with a smooth confinement, Phys. Rev. B **86**, 100503(R) (2012).

[26] J. Cayao, E. Prada, P. San-Jose, and R. Aguado, SNS junctions in nanowires with spin-orbit coupling: Role of confinement and helicity on the subgap spectrum, Phys. Rev. B **91**, 024514 (2015).

[27] P. San-Jose, J. Cayao, E. Prada, and R. Aguado, Majorana bound states from exceptional points in non-topological superconductors, Sci. Rep. **6**, 21427 (2016).

[28] C. Reeg, O. Dmytruk, D. Chevallier, D. Loss, and J. Klinovaja, Zero-energy Andreev bound states from quantum dots in proximitized Rashba nanowires, Phys. Rev. B **98**, 245407 (2018).

[29] O. A. Awoga, J. Cayao, and A. M. Black-Schaffer, Supercurrent Detection of Topologically Trivial Zero-Energy States in Nanowire Junctions, Phys. Rev. Lett. **123**, 117001 (2019).

[30] A. Vuik, B. Nijholt, A. Akhmerov, and M. Wimmer, Reproducing topological properties with quasi-Majorana states, SciPost Phys. **7**, 061 (2019).

[31] A. Aharony, O. Entin-Wohlman, B. I. Halperin, and Y. Imry, Phase measurement in the mesoscopic Aharonov-Bohm interferometer, Phys. Rev. B **66**, 115311 (2002).

[32] N. Read and D. Green, Paired states of fermions in two dimensions with breaking of parity and time-reversal symmetries and the fractional quantum Hall effect, Phys. Rev. B **61**, 10267 (2000).

[33] L. Fu and C. L. Kane, Superconducting Proximity Effect and Majorana Fermions at the Surface of a Topological Insulator, Phys. Rev. Lett. **100**, 096407 (2008).

[34] J. D. Sau, R. M. Lutchyn, S. Tewari, and S. Das Sarma, Generic New Platform for Topological Quantum Computation using Semiconductor Heterostructures, Phys. Rev. Lett. **104**, 040502 (2010).

[35] R. M. Lutchyn, J. D. Sau, and S. Das Sarma, Majorana Fermions and a Topological Phase Transition in Semiconductor-Superconductor Heterostructures, Phys. Rev. Lett. **105**, 077001 (2010).

[36] Y. Oreg, G. Refael, and F. vonOppen, Helical Liquids and Majorana Bound States in Quantum Wires, Phys. Rev. Lett. **105**, 177002 (2010).

[37] C. Mahaux and H. A. Weidenmüller, Comparison between the R-matrix and eigenchannel methods, Phys. Rev. **170**, 847 (1968).

[38] X.-Q. Li and L. Xu, Nonlocality of Majorana zero modes and teleportation: Self-consistent treatment based on the Bogoliubov–de Gennes equation, Phys. Rev. B **101**, 205401 (2020).

[39] R. M. Lutchyn, E. P. A. M. Bakkers, L. P. Kouwenhoven, P. Krogstrup, C. M. Marcus, and Y. Oreg, Majorana zero modes in superconductor–semiconductor heterostructures, Nat. Rev. Mater. **3**, 52 (2018).

[40] A. Y. Kitaev, Unpaired Majorana fermions in quantum wires, Phys. Usp. **44**, 131 (2001).

[41] A. C. Potter and P. A. Lee, Majorana end states in multiband microstructures with Rashba spin-orbit coupling, Phys. Rev. B **83**, 094525 (2011).

[42] M. Tinkham, *Introduction to Superconductivity*, 2nd ed., Dover Books on Physics (Dover, Mineola, NY, 2004).

[43] E. A. Lynton, B. Serin, and M. Zucker, The superconductive critical temperature and the electronic specific heat of impure tin, J. Phys. Chem. Solids **3**, 165 (1957).

[44] A. B. Pippard, The effect of alloying on the superconducting transition temperature of tin, J. Phys. Chem. Solids **3**, 175 (1957).

[45] P. W. Anderson, Theory of dirty superconductors, J. Phys. Chem. Solids **11**, 26 (1959).

[46] L. J. Buchholtz and G. Zwicknagl, Identification of *p*-wave superconductors, Phys. Rev. B **23**, 5788 (1981).

[47] P. Hirschfeld, D. Vollhardt, and P. Wölfle, Resonant impurity scattering in heavy fermion superconductors, Solid State Commun. **59**, 111 (1986).

[48] S. Schmitt-Rink, K. Miyake, and C. M. Varma, Transport and Thermal Properties of Heavy-Fermion Superconductors: A Unified Picture, Phys. Rev. Lett. **57**, 2575 (1986).

[49] K. Maki and E. Puchkaryov, Impurity scattering in isotropic p-wave superconductors, Europhys. Lett. **45**, 263 (1999).

[50] B. Zocher, M. Horsdal, and B. Rosenow, Robustness of topological order in semiconductor–superconductor nanowires in the Coulomb blockade regime, New J. Phys. **15**, 085003 (2013).

[51] F. Braun and J. von Delft, Superconductivity in ultrasmall metallic grains, Phys. Rev. B **59**, 9527 (1999).

[52] S. Das Sarma, J. D. Sau, and T. D. Stanescu, Splitting of the zero-bias conductance peak as smoking gun evidence for the existence of the Majorana mode in a superconductor-semiconductor nanowire, Phys. Rev. B **86**, 220506(R) (2012).